A Three-Phase Modular Isolated Matrix Converter

Usman Nasir, *Student Member, IEEE*, Alessandro Costabeber, *Member, IEEE*, Patrick Wheeler, *Senior Member, IEEE*, Marco Rivera, *Member, IEEE*, and Jon Clare, *Senior Member, IEEE*

***Abstract*—This paper discusses the analysis, design, and experimental validation of a modular isolated matrix converter (MIMC), including modulation, commutation, and control. The MIMC topology is a single-stage high power density ac–ac converter, which is attractive for traction applications and space-restricted low voltage (LV) or medium voltage (MV) future distribution networks. The topology under study utilizes bidirectional switches based dual-active-bridge cells as basic building blocks. A single cell would have limited practical application as the output frequency is locked to the input one. On the contrary, the repetition of single cells proposed in the MIMC extending the matrix converter concept, achieves variable frequency operation while also providing a modular structure. However, the presence of medium frequency transformers in each cell poses additional challenges for modulation and safe commutation that are discussed and solved in this paper. Experimental results from a proof-of-concept 6 kW laboratory scale prototype validate the practical feasibility and the operation of the MIMC.**

***Index Terms*—Bidirectional switches, commutation, direct ac–ac converters, isolated matrix converter, solid-state transformers, venturini modulation.**

I. Introduction

IN 1988, Alesina and Venturini proposed the first direct ac–ac power converter [1], known as matrix converter (MC). In a traditional MC, the output is directly connected to the input side via nine bidirectional switches, avoiding large dc link capacitors and consequently providing a single stage solution with high power density [2] and reliability [3]. The resulting topology is particularly suitable for applications such as integrated motor drives [4].

If the direct ac–ac conversion is intended for traction or interconnection of low voltage (LV) or medium voltage (MV) ac grids, an isolation stage must always be included to prevent fault propagation [5]. Isolation could be provided by adding line

Manuscript received October 9, 2018; revised February 12, 2019; accepted March 29, 2019. Date of publication April 8, 2019; date of current version September 6, 2019. This work was supported by the Newton Picarte and Fondecyt Project under Grant 1160690. Recommended for publication by Associate Editor M. Saeedifard. *(Corresponding author: Usman Nasir.)*

U. Nasir, A. Costabeber, and J. Clare are with the Department of Electrical and Electronic Engineering, University of Nottingham, Nottingham NG7 2RD U.K. (e-mail:

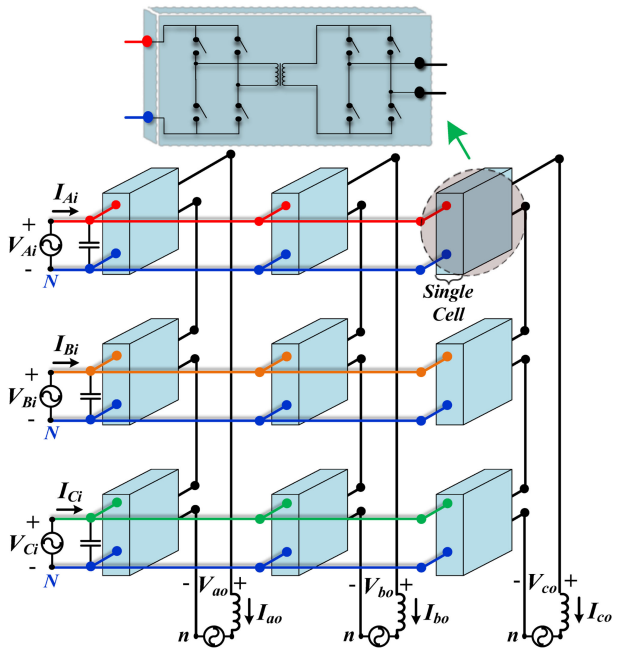

Fig. 1. Modular isolated ac–ac matrix converter-three-phase to three-phase.

Since isolation, modularity, and flexibility are the key requirements of future electrical networks [5], a new single-stage modular isolated matrix converter (MIMC) topology was proposed in [28]. As shown in Fig. 1, the MIMC utilizes the repetition of cells made of two H-bridges with bidirectional switches and a MF transformer to keep modularity intact. The individual cells in the proposed topology correspond to the single-phase to single-phase ac–ac topology discussed in [29]–[32]. The single cell has restricted applications as the output frequency must always match the input one [7]. To be able to achieve output frequency adaptation, in the MIMC each output phase is made by the combination of three independent single-phase to single-phase ac–ac SSTs with a series connection at the secondary side, as shown in Fig. 2.

In the converter arrangement, the output voltage waveform demanded by each output phase can be generated by selecting the most appropriate combination of the available input voltages. As a result, the modulation techniques developed for MC are also applicable to the MIMC. As a result, the behavior of the MIMC at the input and output terminals is the same as the one of an equivalent MC, i.e., it exhibits same characteristics and performance as MC, with the advantage of providing embedded and distributed MF isolation and modularity. Additionally, in the MIMC the semiconductor stresses will be shared between the increased number of devices.

As discussed above, the topology has already been proposed in [28]. However, only the principle of operation and a preliminary set of simulations were discussed. The aim of this paper is to demonstrate the practical viability of the MIMC topology, providing a detailed discussion about modulation and commutation—the latter is particularly challenging because of leakage inductances, as discussed later—and providing experimental results from a laboratory-scale prototype. Considering that the three output phases are independent, the analysis

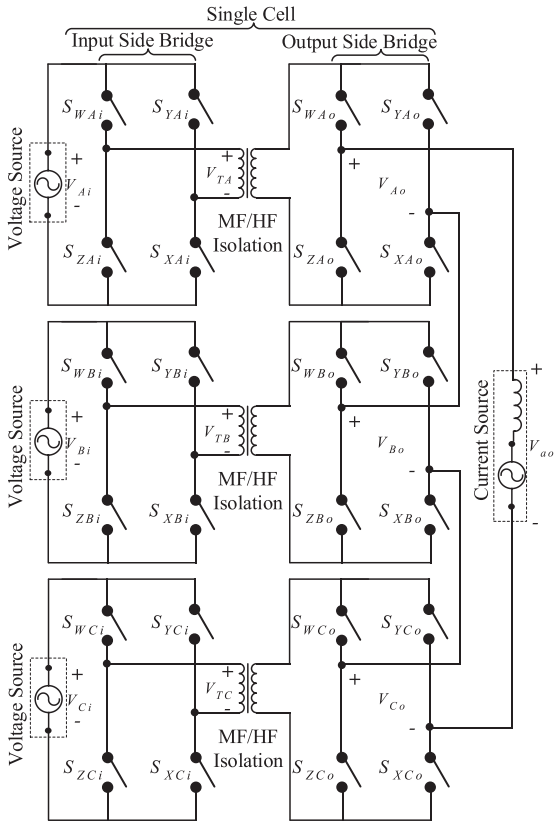

Fig. 2. Three-phase to single-phase section of the MIMC.

and the experimental validation will refer to one of the three-phase to single-phase sections of the MIMC shown in Fig. 2. Note that the structure presented in Fig. 1 can be extended to higher voltage and power. This extension can be done by determining the number of cells N based on the required voltage level and then a cascade connection of N cells can be inserted into the structure of Fig. 1 to share in the input voltage V_{Ki}.

The rest of the paper is organized as follows. The modulation and commutation methods are presented in Sections II and III, respectively. The simulation and experimental validation of the proposed system are discussed in Sections IV and V, respectively. Finally, the conclusions of study are presented in Section VI.

II. Modulation Technique

In order to use MC modulation techniques, such as 50% Venturini modulation, with the MIMC the first step is the identification of the modulation states (MS) available in the topology. Considering the H-bridges in Fig. 2, with a voltage source at the input, a current source at the output, and an ideal MF transformer, the generic MS matrices of the H-bridges can be defined as (1), where "i" indicates the input side, "o" the output side and "K" the three input phases $K = A, B, C$.

Subsequently, to respect the constraints that the input voltage sources cannot be short circuited and that the output current source cannot be open circuited during operation [33], the three MS matrices available for modulation can be written as in (2). MS_1 and MS_2 are the two active states whereas MS_0 is a zero

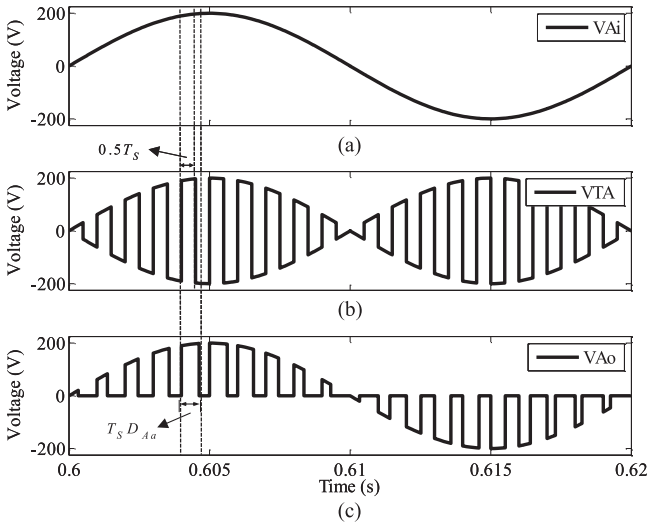

Fig. 3. Theoretical voltage waveforms in a single-cell as a result of 50% Venturini modulation. (a) Input voltage V_{Ai}. (b) Transformer voltage V_{TA}. (c) Output voltage V_{Ao}.

state matrix. Note that the zero state can be implemented with two different MS matrices that however have the same effect on the modulation waveforms

$$\mathrm{MS}_{Ki} = \begin{bmatrix} S_{\mathrm{WKi}} & S_{\mathrm{YKi}} \\ S_{\mathrm{ZKi}} & S_{\mathrm{XKi}} \end{bmatrix}$$

$$\mathrm{MS}_{\mathrm{Ko}} = \begin{bmatrix} S_{\mathrm{WKo}} & S_{\mathrm{YKo}} \\ S_{\mathrm{ZKo}} & S_{\mathrm{XKo}} \end{bmatrix} \tag{1}$$

$$\mathrm{MS}_1 = \begin{bmatrix} 1 & 0 \\ 0 & 1 \end{bmatrix}, \quad \mathrm{MS}_2 = \begin{bmatrix} 0 & 1 \\ 1 & 0 \end{bmatrix}$$

$$\mathrm{MS}_0 = \begin{bmatrix} 0 & 0 \\ 1 & 1 \end{bmatrix} \quad \text{or} \quad \begin{bmatrix} 1 & 1 \\ 0 & 0 \end{bmatrix}. \tag{2}$$

The basic operation of the MIMC is achieved first converting the low-frequency input voltage waveform into a 50% duty cycle MF voltage waveform as shown in Fig. 3(b), by simply flipping the input voltages at the switching frequency f_{sw}. This is equivalent to implementing the switching function (3) on the three input side bridges. Where T_S is the switching period, and the equation is written for brevity only for the first period $0 < t < T_S$. The same compact notation will be adopted also for in the other equations. From (3), it can be observed that the state MS_1 will be applied for the first half of the switching period, i.e., from 0 to $0.5T_S$ making $V_{TK} = V_{Ki}$ whereas state MS_2 for the other half of the switching period, i.e., from $0.5T_S$ to T_S making $V_{TK} = -V_{Ki}$ and, therefore, all the input side bridges are generating a 50% duty cycle MF waveform at their transformer terminals

V_{TK}	MS_{Ki}	Condition
V_{Ki}	MS_1	$0 \le t \le 0.5T_S$
$-V_{Ki}$	MS_2	$0.5T_S < t \le T_S$

. (3)

A 50% duty cycle waveform at the transformer has been selected as it minimizes the transformer flux variation. It can be noted from (3) that all the three input bridges are commutated synchronously. In general, this is not a strict requirement and different phases could be flipped in different time instants without affecting the average components of the modulated waveforms. On the other hand, the harmonic content of the waveforms would be affected. These aspects are not further discussed in this paper to keep the focus on the basic modulation strategy and to simplify the graphical representation of the switching waveforms.

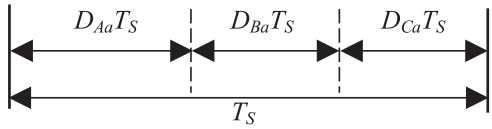

Fig. 4. Arrangement of the duty cycles in a three-phase to single-phase MC.

The 50% duty cycle modulation of the input side bridges is only meant to provide a suitable voltage waveform to the MF transformers, regardless the value of the modulation wave. Instead, the output bridge voltages V_{Ko} in Fig. 2 are defined by the 50% Venturini modulation according to (4), where D_{kj} is the duty cycle of the input phase K in the generation of the output voltage j. It can be observed from (4)–(6) that the equations are the same as the ones used in standard MCs, where the time during which each of the input phases contributes to the output voltage is defined by the Venturini modulation

$$D_{Kj} = \frac{1}{3}\left(1 + \frac{2\, V_{Ki} V_{jo}}{{V_m}^2}\right) \tag{4}$$

$$V_{Ki} = V_m \sin\left(\omega_i t + \phi_K\right) \tag{5}$$

$$V_{jo} = q V_m \sin\left(\omega_o t + \phi_j\right) \tag{6}$$

where V_{Ki}, $K = A, B, C$ and V_{jo}, $j = a, b, c$ are the three-phase input and output voltages, respectively. For the simplified three-phase to single-phase system under study, only $j = a$ is considered. The duty cycle arrangement in this simplified case is illustrated in Fig. 4. The duty cycle arrangement of Fig. 4 can be attained by implementing the switching functions (7)–(9) in each of the output side bridges of the MIMC. The switching function (7) will be applied to the output bridge of the top cell. In (7), the duty cycle D_{Aa} can be less than or equal to 0.5, i.e., $D_{Aa}T_S \le 0.5T_S$ or greater than 0.5, i.e., $D_{Aa}T_S > 0.5T_S$. In case the duty cycle D_{Aa} is below or equal to 0.5, the condition $D_{Aa}T_S \le 0.5T_S$ becomes valid and two intervals are possible in (7) based on which the two steady states, i.e., MS_1 and MS_0 will be applied. In short, if the condition $D_{Aa}T_S \le 0.5T_S$ is satisfied, then the active state MS_1 will be applied for a duration or interval of $0 \le t \le D_{Aa}T_S$ and state MS_0 will be applied for the remaining interval $D_{Aa}T_S < t \le T_S$. Similarly, the switching function (8) will be applied to output bridge of middle cell. For instance if the first condition, i.e., $D_{Aa}T_S \le 0.5T_S \le (D_{Aa} + D_{Ba})T_S$ is true in (8) then there are a total of four intervals in which the state MS_0 will be applied for the interval $0 \le t \le D_{Aa}T_S$, MS_1 for interval $D_{Aa}T_S < t \le 0.5T_S$, MS_2 for interval $0.5T_S < t \le (D_{Aa} + D_{Ba})T_S$ and again MS_0 for the remaining interval $(D_{Aa} + D_{Ba})T_S < t \le T_S$. The other

conditions and interval of all the switching functions in (7)–(9) can be interpreted following the discussed approach.

It is important to note that (7)–(9) are written under the assumption that all the input bridges are flipped synchronously, and therefore the voltage applied to each of the MF transformer primaries V_{TK} and modulated by the output bridges equals the corresponding phase voltage V_{Ki} for the first half of the switching period and V_{Ki} for the other half.

Fig. 3 shows the basic waveforms for the top cell in Fig. 2 as a result of the switching functions given in (3) and (7)–(9). The cell output voltages V_{Ko} as a result of the switching functions are presented in Fig. 5. It is important to note, from Fig. 5, that the total output voltage V_{ao} is the sum of the individual output voltages of the cells. This is because of the series connection of the output side bridges in the three-phase to single-phase system of Fig. 2, the cell voltages V_{Ko} (7)–(9) shown at the bottom of this page, depicted in Fig. 5, are summed as shown in (10) to generate the total output voltage V_{ao}. The instantaneous output voltage V_{ao} can also be rewritten as (11), which means that the input voltage V_{Ai} will appear at the output, i.e., $V_{ao} = V_{Ai}$ for a duration of $0 \leq t \leq D_{Aa}T_S$ V_{Ai} and so on thus follows the arrangement of MCs shown in Fig. 4

$$V_{ao} = \sum_{K=A,B,C} V_{Ko} = V_{Ao} + V_{Bo} + V_{Co} \tag{10}$$

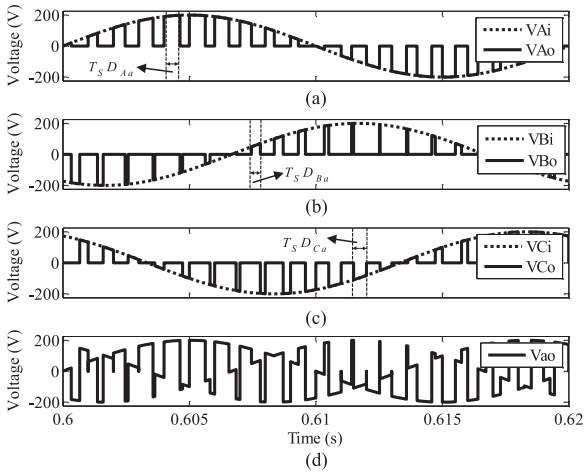

Fig. 5. Theoretical voltage waveforms in the three-phase to single-phase MIMC as a result of 50% Venturini modulation. (a)–(c) Input and output voltages of the cells V_{Ki} and V_{Ko}. (d) Total output voltage V_{ao} of (10).

$$V_{ao} = \left\{ \begin{array}{c|c} \text{Voltage} & \text{Interval} \\ \hline V_{Ai} & 0 \leq t \leq D_{Aa}T_S \\ V_{Bi} & D_{Aa}T_S < t \leq (D_{Aa} + D_{Ba})\,T_S \\ V_{Ci} & (D_{Aa} + D_{Ba})\,T_S < t \leq T_S \end{array} \right\}. \tag{11}$$

V_{Ao}	MS_{Ao}	Interval	Condition
V_{Ai}	MS_1	$0 \leq t \leq D_{Aa}T_S$	$D_{Aa}T_S \leq 0.5T_S$
0	MS_0	$D_{Aa}T_S < t \leq T_S$	
V_{Ai}	MS_1	$0 \leq t \leq 0.5T_S$	$D_{Aa}T_S > 0.5T_S$
V_{Ai}	MS_2	$0.5T_S < t \leq D_{Aa}T_S$	
0	MS_0	$D_{Aa}T_S < t \leq T_S$	

(7)

V_{Bo}	MS_{Bo}	Interval	Condition
0	MS_0	$0 \leq t \leq D_{Aa}T_S$	
V_{Bi}	MS_1	$D_{Aa}T_S < t \leq 0.5T_S$	$D_{Aa}T_S \leq 0.5T_S$
V_{Bi}	MS_2	$0.5T_S < t \leq (D_{Aa} + D_{Ba})T_S$	$\leq (D_{Aa} + D_{Ba})T_S$
0	MS_0	$(D_{Aa} + D_{Ba})T_S < t \leq T_S$	
0	MS_0	$0 \leq t \leq D_{Aa}T_S$	$0.5T_S \leq D_{Aa}T_S$
V_{Bi}	MS_2	$D_{Aa}T_S < t \leq (D_{Aa} + D_{Ba})T_S$	
0	MS_0	$(D_{Aa} + D_{Ba})T_S < t \leq T_S$	
0	MS_0	$0 \leq t \leq D_{Aa}T_S$	$(D_{Aa} + D_{Ba})T_S$
V_{Bi}	MS_1	$D_{Aa}T_S < t \leq (D_{Aa} + D_{Ba})T_S$	$\leq 0.5T_S$
0	MS_0	$(D_{Aa} + D_{Ba})T_S < t \leq T_S$	

(8)

V_{Co}	MS_{Co}	Interval	Condition
0	MS_0	$0 \leq t \leq (D_{Aa} + D_{Ba})T_S$	$(D_{Aa} + D_{Ba})T_S$
V_{Ci}	MS_1	$(D_{Aa} + D_{Ba})T_S < t \leq 0.5T_S$	$\leq 0.5T_S$
V_{Ci}	MS_2	$0.5T_S < t \leq T_S$	
0	MS_0	$0 < t \leq (D_{Aa} + D_{Ba})T_S$	$(D_{Aa} + D_{Ba})T_S$
V_{Ci}	MS_2	$(D_{Aa} + D_{Ba})T_S < t \leq T_S$	$> 0.5T_S$

(9)

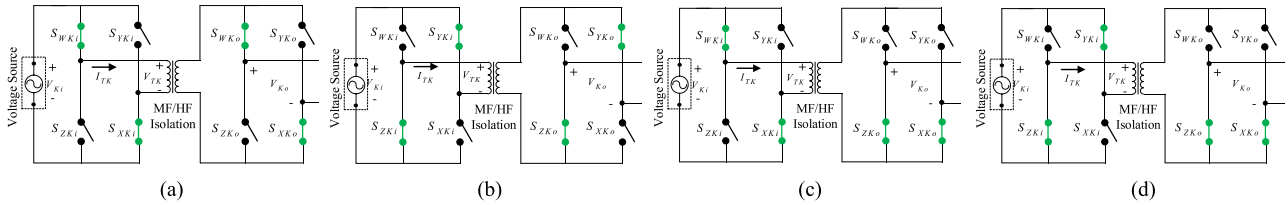

Fig. 6. States required in a single-cell for the implementation of 50% Venturini modulation. (a) Modulation state MS_1MS_1. (b) Modulation state MS_2MS_2. (c) Modulation state MS_1MS_0. (d) Modulation state MS_2MS_0.

For the practical implementation of (7)–(9), the required states in each of the cells in Fig. 2 are $MS_{Ki}MS_{Ko}$= [MS_1MS_1, MS_2MS_2, MS_1MS_0, MS_2MS_0] and are illustrated in Fig. 6(a)–(d), respectively. The output voltage waveforms—as well as input and output currents—have harmonic content that can be derived analytically by applying the approach proposed in [34]. Considering that the output voltage spectrum of the MIMC is the same as the one of the standard MC, discussion about harmonics in this paper is limited to the transformer voltages V_{TK}, whose Fourier series, shown in (12), is essential for the MF transformer design. Instead, the harmonic spectrum of the cell output voltages V_{Ko} given in (7)–(9), is only used for the validation of the modulation method. By neglecting the switching harmonics, the low-frequency components of the individual cell voltages V_{Ko} are given in (13). Due to the series connection at the output side, these components reduce to the desired fundamental (14) as the other terms in V_{ao} cancel in the sum. Equation (14) confirms that 50% Venturini modulation is applicable to the three-phase to single-phase MIMC. Note that the theoretical derivation of (12) and (13) is given in Appendix

$$V_{TK}(t) = \frac{2V_m}{\pi} \sum_{n=1,3,5,\ldots}^{\infty} \frac{1}{n} (\cos(n\omega_s t - \omega_i t - \phi_K) - \cos(n\omega_s t + \omega_i t + \phi_K)) \tag{12}$$

$$V_{Ko}(t) = \frac{V_m}{3}\sin(\omega_i t + \phi_K) + \frac{qV_m}{6}\sin(2\omega_i t - \omega_o t - \phi_K) - \frac{qV_m}{6}\sin(2\omega_i t + \omega_o t - \phi_K) + \frac{qV_m}{3}\sin(\omega_o t) \tag{13}$$

$$V_{ao}(t) = \sum_{K=A,B,C} V_{Ko}(t) = qV_m \sin(\omega_o t). \tag{14}$$

The voltage regulation ratio of the MIMC is dependant on the turn ratio of the MF transformer but assuming turn ratio of the transformer to be unity, a maximum-voltage regulation ratio of 0.86 can be achieved by modifying the duty cycle (4) to inject third harmonic.

So far, the analysis of the modulation technique for the MIMC has assumed ideal semiconductor devices, characterized by instantaneous switching. In addition, the MF transformer has been considered ideal, with zero leakage inductance. When implementing the modulation in a practical converter, the two assumptions lose validity and the modulation must be augmented by a suitable strategy to guarantee safe commutation of the bidirectional switches. Switching times can be easily taken into account by implementing a modified version of the four-step commutation used in MC [2]. Instead, taking into account a non-zero leakage inductance of the MF transformer is a more challenging aspect, discussed in detail in the following section.

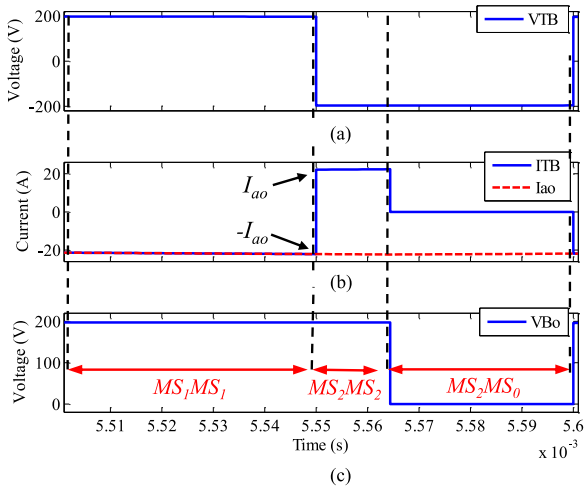

Fig. 7. Example of ideal transformer current in a single cell operated with the states required by 50% Venturini modulation zero leakage transformer. (a) Transformer voltage V_{TB}. (b) Current I_{TB}. (c) Output voltage V_{Bo}.

III. Commutation Method

In MCs, the commutation method is designed to safely change the state of the bidirectional switches without open circuiting the output currents or short circuiting the input voltage sources.

In the MIMC, each bridge can achieve independent four-step commutation method, as presented in [29], only if the impact of the MF transformer leakage inductance is neglected. However, with non-negligible leakage inductance, the standard four-step commutation method can cause overvoltage across the semiconductor devices when a commutation of an output bridge in one of the cells occurs. This because a commutation of the output bridge requires a sudden reversal of the current through the leakage inductance I_{TK}, which always flips between $+I_{ao}$ (grid current) and $-I_{ao}$ depending on the state of the output bridge.

To highlight this phenomenon, an example of the ideal commutation waveforms in a single cell during a switching period of T_S are shown in Fig. 7. It can be seen that the state transition from MS_1MS_1 to MS_2MS_2 is requiring the transformer current I_{TB} to undergo sudden reversal from $-I_{ao}$ and $+I_{ao}$, which will generate a voltage spike in a practical transformer where leakage inductance is non-negligible. A detailed discussion about the impact of the leakage inductance on the commutation process can be found in [35]. The consequence is that the standard four-step commutation can be applied to the MIMC only if

all the bridges have dissipative clamps to protect them against overvoltage. This causes additional loss as the clamp circuit will be triggered every time the modulator requires a state change that corresponds to a reversal of the leakage inductance current. Reduction of leakage inductance [29] can mitigate but not eliminate the problem. To achieve safe commutation, various commutation methods have been reported in literature [36]–[39], which suggest the use of additional capacitor either in parallel [38] or in series [39] to transformer. However, these options come at the cost of reduced power density and increased power losses.

A. Leakage-Tolerant Source-Based Commutation Method

A solution to the commutation problem has been recently discussed in [35], where the analysis is focused on a single cell of the MIMC converter in Fig. 2. The paper proposed the exploitation of additional states available in the converter that would not be necessary in ideal conditions but become essential when dealing with the leakage inductance issue. Nasir *et al.* [35] proposes the introduction of a *current decoupling phase*, where the output bridge is temporarily put in an controlled short circuit state during which the leakage inductance current is reversed, driven by the input voltage. The converter states are selected so that the temporary output short naturally terminates when the leakage inductance current matches the value of the output current. For this reason the short is *controlled* and does not require any high bandwidth current measurement but only an appropriate fixed timing of the commutation sequence. The method guarantees safe commutation without triggering the protection clamps for most of the line period, except during the intervals where the available input voltage is not enough to drive the leakage inductance current, i.e., around the zero crossings of the input voltage

$$\mathrm{CS}_{Ki} = \begin{bmatrix} S_{WK_{0i}} S_{WK_{1i}} & S_{YK_{0i}} S_{YK_{1i}} \\ S_{ZK_{0i}} S_{ZK_{1i}} & S_{XK_{0i}} S_{XK_{1i}} \end{bmatrix}$$

$$\mathrm{CS}_{\mathrm{Ko}} = \begin{bmatrix} S_{WK_{0o}} S_{WK_{1o}} & S_{YK_{0o}} S_{YK_{1o}} \\ S_{ZK_{0o}} S_{ZK_{1o}} & S_{XK_{0o}} S_{XK_{1o}} \end{bmatrix} \tag{15}$$

$$A = \begin{bmatrix} 11 & 00 \\ 00 & 11 \end{bmatrix}, \quad B = \begin{bmatrix} 10 & 00 \\ 00 & 10 \end{bmatrix}, \quad C = \begin{bmatrix} 01 & 00 \\ 00 & 01 \end{bmatrix},$$

$$D = \begin{bmatrix} 00 & 11 \\ 11 & 00 \end{bmatrix}, \quad E = \begin{bmatrix} 00 & 10 \\ 10 & 00 \end{bmatrix}, \quad F = \begin{bmatrix} 00 & 01 \\ 01 & 00 \end{bmatrix},$$

$$G = \begin{bmatrix} 11 & 01 \\ 01 & 11 \end{bmatrix}, \quad H = \begin{bmatrix} 10 & 01 \\ 01 & 10 \end{bmatrix}, \quad I = \begin{bmatrix} 00 & 00 \\ 01 & 10 \end{bmatrix},$$

$$J = \begin{bmatrix} 00 & 00 \\ 11 & 11 \end{bmatrix}, \quad K = \begin{bmatrix} 01 & 10 \\ 10 & 01 \end{bmatrix}, \quad L = \begin{bmatrix} 01 & 11 \\ 11 & 01 \end{bmatrix},$$

$$M = \begin{bmatrix} 01 & 01 \\ 01 & 01 \end{bmatrix}, \quad N = \begin{bmatrix} 10 & 10 \\ 10 & 10 \end{bmatrix}, \quad O = \begin{bmatrix} 00 & 00 \\ 00 & 00 \end{bmatrix},$$

$$Q = \begin{bmatrix} 00 & 00 \\ 10 & 01 \end{bmatrix}, \quad R = \begin{bmatrix} 10 & 11 \\ 11 & 10 \end{bmatrix}. \tag{16}$$

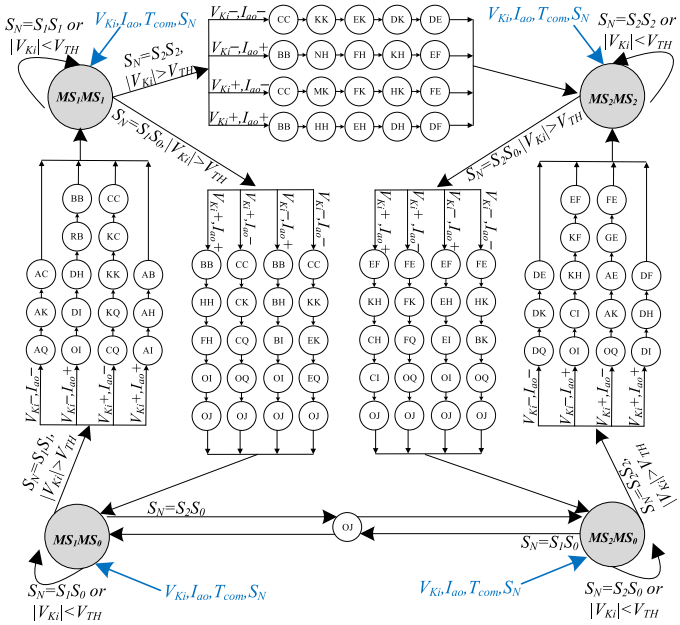

Fig. 8. FSM for implementing the source-based commutation of on single-cell of the proposed MIMC.

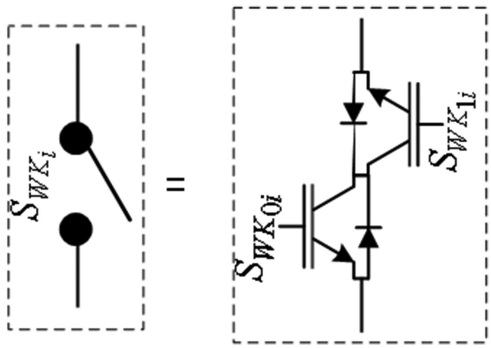

Fig. 9. Representation of an equivalent four-quadrant or bidirectional switch.

Based on the leakage-inductance-tolerant commutation scheme discussed in [35], a finite state machine (FSM) has been implemented as shown in Fig. 8 to move between the steady states of Fig. 6. In the proposed FSM, the commutation paths are represented by arrows, temporary commutation states by small circles and steady states by large grey circles. In the same way as MS matrices, input and output bridge commutation state (CS) matrices of single cell can be represented by (15) where each bidirectional switch is composed of two IGBTs. For instance, S_{WKi} contains S_{WK0i} and S_{WK1i} in the common-collector configuration as shown in Fig. 9. The definition of the CS matrices is reported in (16). The state change variable S_N stores the information regarding the required next steady state. T_{comm} controls the time delay between the commutation states and for the sake of simplicity, the delay time T_{comm} was fixed for all the commutation steps. For instance, assume that the FSM is in commutation state BB then a counter will be started and will keep counting until it reaches the value equal that of T_{comm} and once the counter has reached T_{comm}, FSM will move to next commutation state, i.e., HH, which resets the counter to zero.

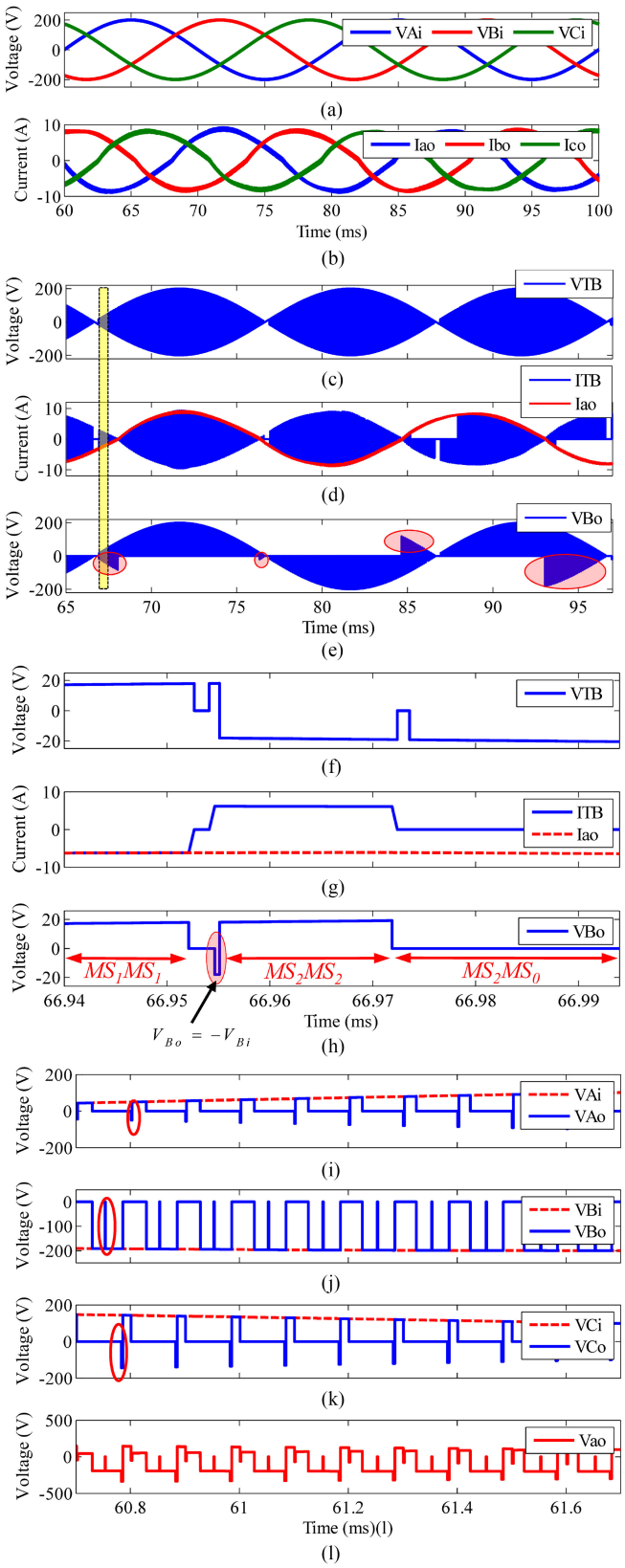

Fig. 10. Open-loop simulated waveforms at different points in the proposed three-phase to three-phase MIMC with Venturini modulation and leakage-tolerant commutation method. (a) and (b) three phase input voltages V_{Ki} and output currents I_{jo}. (c)–(e) Waveforms in the second cell of Fig. 2. (f)–(h) Zoom on the highlighted region in (c)–(e), showing non-ideal commutations. (i)–(l) Cell output voltages V_{Ko} and total output voltage V_{ao}.

TABLE I
SIMULATION PARAMETERS

Parameter	Symbol	Value
Input Frequency	f_i	50 Hz
Output Frequency	f_o	60 Hz
Input Voltage Amplitude	V_{Ki}	200 V (PEAK)
Load Resistance	R	10 Ω
Load Inductance	L	10 mH
Switching Frequency	f_{sw}	10 kHz
Voltage Regulation Ratio	q	0.45
Leakage Inductance	L_{leak}	2.5 μH

For V_{Ki} and I_{ao} represent the input voltages and output current, respectively. A detailed discussion on how the safe commutation is performed has already been presented in [35] and will not be discussed here. However, following the approach of [35], all the paths of FSM have been derived to guarantee safe commutation that can be verified from the results in the following sections.

IV. SIMULATION RESULTS

This section presents in Fig. 10, the results from a full three-phase to three-phase open-loop PLECS simulation of the MIMC. The simulation parameters are shown in Table I. The model includes the leakage-inductance-tolerant commutation scheme, whose effects on the total harmonic distortion (THD) of the output current in open loop has been evaluated as a function of the selected switching frequency, in the simplified assumption that the commutation time T_{comm} is kept constant.

The MIMC operates with a fundamental frequency of 50 Hz at the input and 60 Hz at the output. This test case has been selected to show the applicability of the proposed system in applications requiring frequency decoupling, e.g., 50 and 60 Hz grids or 50, 25, and 16.7 Hz traction systems [10].

Fig. 10(a) and (b) presents the three-phase input voltages V_{Ki} and the output currents I_{jo} recorded in the three-phase to three-phase MIMC. By observing the period of the voltages V_{Ki} and currents I_{jo} in Fig. 10(a) and (b), three-phase operation of MIMC while achieving frequency adaptation can be confirmed. However, it must be noted from Fig. 10(b) that the output currents I_{jo} are experiencing distortion, which is associated with the leakage-inductance-tolerant commutation scheme. To illustrate the impact of commutation scheme, switching voltages and currents of a single cell are presented in Fig. 10(c)–(e). By comparing the output voltage of cell V_{Bo}, given in Fig. 10(e), with the ideal case, shown in Fig. 5(b), it can be noted that the red circles of Fig. 10(e) highlight the distortion added due to non-ideal commutation. To clearly illustrate the commutation-related distortion, a zoomed view of the highlighted-yellow-region in Fig. 10(c)–(e) is presented in Fig. 10(f)–(h), which shows two non-ideal state transitions, from MS_1MS_1 to MS_2MS_2 and then from MS_2MS_2 to MS_2MS_0.

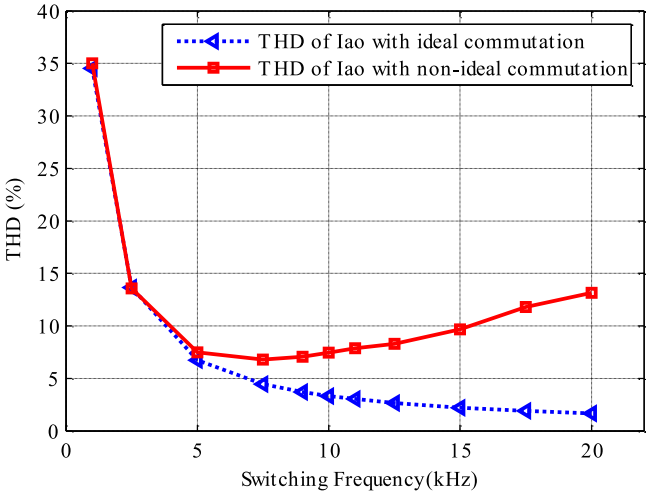

Fig. 11. Switching frequency versus THD with a fixed commutation time and filter inductor $L = 10$ mH in the open-loop MIMC.

Looking at the first commutation, i.e., from MS_1MS_1 to MS_2MS_2 in Fig. 10(h), it can be observed that the output voltage V_{Bo} has commutation-associated distortion, i.e., the pulse $V_{Bo} = -V_{Bi}$, which is highlighted in red region. By comparing non-ideal waveforms of Fig. 10(f)–(h) with the ideal waveforms given in Fig. 7(a)–(c), it can be confirmed that the distortion is associated with the commutation. The said distortion, highlighted in Fig. 10(h), happens when the leakage inductance L_{leak} has been fully charged to $+I_{ao}$ and the converter is waiting for the next commutation state because a fixed commutation step T_{comm} is used. Thus, the duration of the distortion is dependent on the leakage inductance charging time, which varies with the operating point, i.e., depends on the magnitude of instantaneous values of input voltage V_{Ki} and output current I_{ao}. During the commutation process, the converter goes through various commutation states. For instance, the commutation under discussion takes the commutation states CC, MK, FK, HK, FE of the FSM given in Fig. 8.

It is important to mention that the output voltage distortion includes a low-frequency component, a dominant component at the output frequency and multiples. For the sake of understanding the operation of the converter, only few 50 Hz cycles are adequate, as shown in the simulated results of Fig. 10(a)–(e), thus the period of I_{TB} is not fully visible in Fig. 10(d).

To highlight, how the switching output voltage V_{ao} will look with the commutation method, cell voltage V_{Ko} waveforms are presented in Fig. 10(i)–(l). The detailed discussion on which commutation states are causing the distortion can be found in [35] and will not be discussed here.

In order to quantify the distortion associated with the commutation, the MIMC was operated with ideal as well as non-ideal commutation scheme and the THD of the output current I_{ao} was observed at various switching frequencies as shown in Fig. 11. It can be observed from Fig. 11 that in ideal case, the THD of the output current I_{ao} always has an inverse relation with the switching frequency f_{sw} but this is not true for non-ideal case. Up till a switching frequency f_{sw} of 5 kHz, the THD of both cases remain almost same as the fixed commutation time

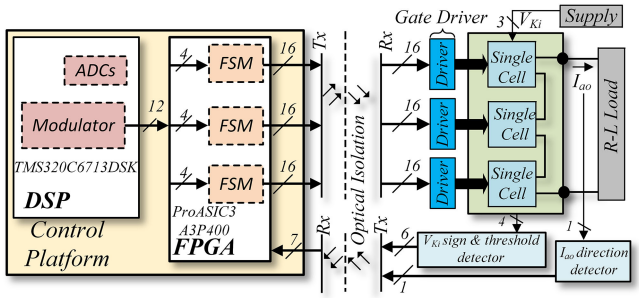

Fig. 12. Block diagram of the experimental setup for the three-phase to single-phase MIMC topology.

is negligible compared to the switching period but with the further increase of switching frequency f_{sw}, the fixed commutation time becomes significant part of the switching period, therefore, causing the THD to increase. The observed optimum range of operation for the MIMC is from 5 to 10 kHz. Within the optimum range, a higher switching frequency f_{sw} will be preferred as the size of the magnetic components, i.e., MF transformer will reduce. Therefore, a switching frequency f_{sw} of 10 kHz was selected in simulation as well as in the experimental setup.

V. Experimental Setup and Validation

To validate the operation of the proposed MIMC topology, a 6 kW proof-of-concept laboratory scale prototype of the three-phase to single-phase MIMC was built. The block diagram of experimental setup is shown in Fig. 12. A custom digital signal processor (DSP)/field programmable gate array (FPGA) control platform, using a TMS320C6713DSK DSP and a ProASIC3 FPGA, has been used. Since there are four modulation states of each single cell, as shown in Fig. 6, the DSP is implementing the switching functions of (7)–(9) by generating a total of 12 *one-hot encoded* modulation signals for three cells, i.e., four modulation signals per single cell. The modulation signals are fed to the FPGA where a VHDL-based-FSM generates 16 independent gate signals per cell, based on the direction of output current I_{ao}, sign and threshold of input voltages V_{Ki}, to perform the leakage-inductance-tolerant commutation. *V_{Ki} sign and threshold detector* block receives four electrical cables as the input voltage V_{Ki} is a three-phase four-wire system. The said block feeds six optical signals to the FPGA, out of which three contain the information of sign and the remaining three contains the information of the threshold. The threshold of the input voltages is detected to avoid commutation when the input voltage magnitude is below the set threshold. This can be observed in the simulation result of Fig. 10(d) where current I_{TB} is zero, i.e., no commutation is performed at the instants when magnitude of voltage V_{TB} is close to zero. The value of threshold can be set by taking into account the peak value of current I_{ao}, leakage inductance L_{leak}, commutation time T_{comm}, and using simple formula $V_{TH} = \frac{\Delta I_{ao} L_{\text{leak}}}{T_{\text{comm}}}$ where $\Delta I_{ao} = 2I_{ao}$ as leakage current changes between I_{ao} and $-I_{ao}$. A total of 48 independent gate signals for three cells, generated by the FPGA, are then optically transmitted to the gate drivers of the SEMIKRON SKM150GM12T4G IGBT modules in the cells.

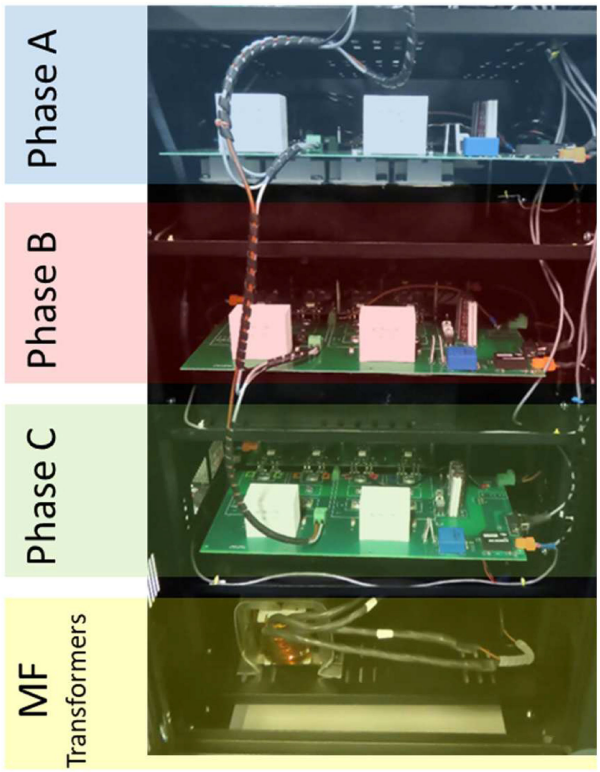

Fig. 13. Photo of the experimental prototype for three-phase to single-phase MIMC topology based on Semikron SKM150GM12T4G modules.

TABLE II
TRANSFORMER PARAMETERS

Parameter	Value
Core Material and shape	2xAMCC125 C-cores
	Amorphous alloy 2605SA1
Leakage Inductance	$4\,\mu$H
Magnetizing Inductance	2.3 mH
Operating Frequency	10 kHz
Number of Turns	16
Turns Ratio	1:1
RMS current	20 A
RMS voltage	400 V
Power rating	8 kVA

Fig. 13 shows the proof-of-concept experimental rig in which three single cells are stacked. Each cell is made of two bidirectional bridges and a MF transformer. For the design of MF isolation transformer, the minimum core area $A_{c\_\min}$ required, to accommodate the flux produced by the 50 duty cycle transformer voltage V_{TK} of (12), can be calculated using (17) where N represents the number of turns, $B_{\max}$ is the flux density of the core material, V_m is the peak of the transformer voltage, ω_s represents switching frequency, and ω_i is the input frequency. A MF transformer, with parameters reported in Table II, was designed to meet $A_c > A_{c\_\min}$. However, the design has not been optimized for the topology under study as the experimental prototype is a flexible rig to test various topologies. It is important to mention that filter capacitors C_F, listed in III, are of polypropylene film type and are added to suppress the voltage spikes generated due to the switching current [40] through line inductance and to exhibit voltage source properties at the input side

$$A_{c\_\min} = \frac{4V_m\omega_s}{NB_{\max}\pi} \sum_{n=1,3,5,\ldots}^{\infty} \frac{1}{n^2{\omega_s}^2 + {\omega_i}^2}. \qquad (17)$$

TABLE III
EXPERIMENTAL TEST PARAMETERS

Parameter	Symbol	Value
Input Voltage Amplitude	V_{Ki}	120 V (RMS)
Frequency at the input side	f_i	50 Hz
Frequency at the output side	f_o	60 Hz
Switching Frequency	f_{sw}	10 kHz
Load Resistance	R	$1.5\,\Omega$
Load Inductance	L	10 mH
Input Filter Capacitance	C_F	$30\,\mu$F

To validate the concept of the proposed topology, the experimental setup was first tested in the open-loop mode to modulate a 60 Hz output from 50 Hz input. This test case has been considered to keep the results consistent with the ones in Section IV.

The setup was operated with the parameters reported in Table III and the recorded experimental waveforms are presented in Fig. 14. From Fig. 14(a), it is important to note that the fundamental component of all the three-phase input voltages V_{Ki} is at 50 Hz whereas that of the filtered output current I_{ao} is at 60 Hz. Note that the current I_{ao} is the average of the pulsewidth-modulated output voltage V_{ao}. This confirms that the MIMC is able to achieve frequency decoupling by following (13) as the components except at $\omega_o t$, i.e., $\omega_i t + \phi_K$ and $2\omega_i t \pm \omega_o t - \phi_K$ are cancelled due to the phase difference of $\frac{2\pi}{3}$. Note that the experimental setup is only a three-phase to single-phase MIMC and, hence, the input side currents I_{Ki} are not sinusoidal, causing distortions in the input voltages V_{Ki}, which will be mitigated in the full three-phase version.

Fig. 14(b) shows several cycles of the modulated output voltages of the individual cells V_{Ko} as well as the sum of these voltages, which is the output voltage V_{ao}. At any time *"t"* the output voltage V_{ao} is the sum of the cell voltages V_{Ko} and follows (14) and this can be validated from Fig. 14(c), which is the zoomed view of the highlighted region of Fig. 14(b). A single switching period T_S has been shown in Fig. 14(c) to clearly indicate that the duty cycles D_{Ka} are arranged in the pattern of D_{Aa}, D_{Ba}, D_{Ca} and are in accordance with the arrangement given in Fig. 4. Furthermore, note that the red regions in the results of Fig. 14(b) highlight the distortion added in the output voltages of cells V_{Ao}, V_{Bo}, V_{Co} due to the commutation. These commutation related distortions in the proposed topology are analogous to the dead-time distortion in the standard

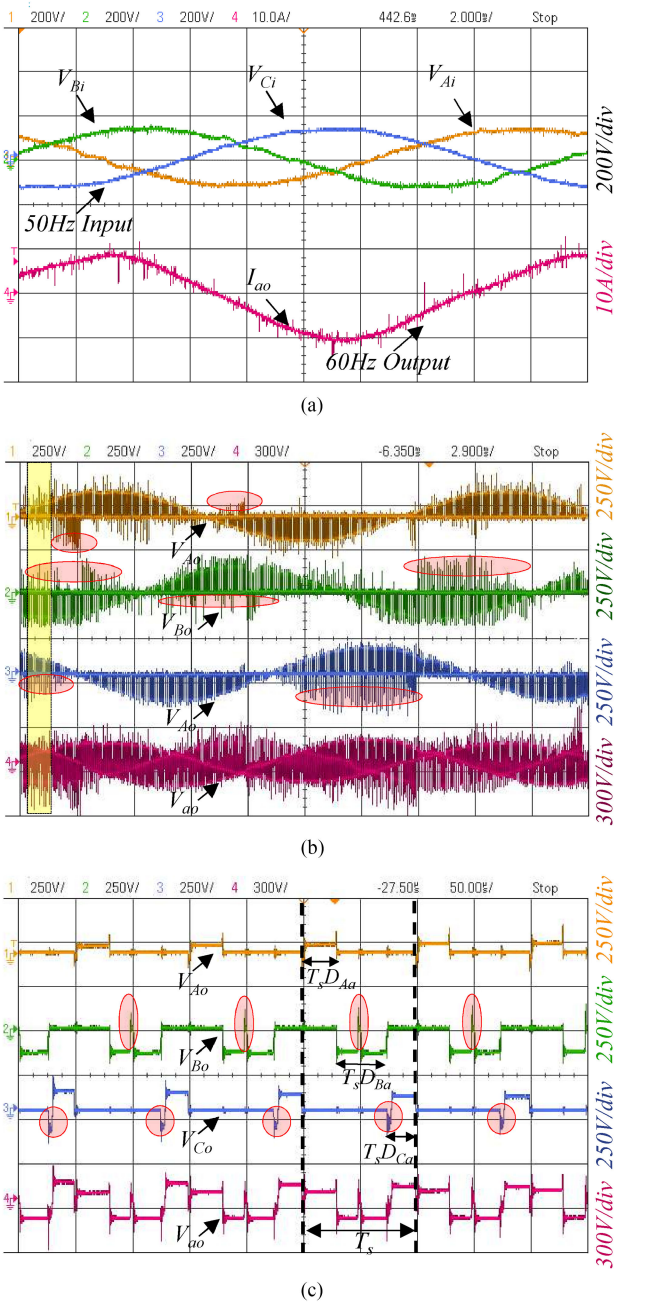

Fig. 14. Open-loop experimental waveforms in a three-phase to single-phase MIMC. (a) Three-phase input voltages V_{Ki} at 50 Hz and output current I_{ao} at 60 Hz. (b) Individual cell voltages V_{Ko} and total output voltage V_{ao}. (c) Zoom of region highlighted in (b), demonstrating that the output voltage V_{ao} is the sum of the individual cell voltages V_{Ko}.

two-level inverters, with the difference that the commutation in the MIMC is also generating low-frequency components. The zoomed view, presented in Fig. 14(c) confirms that the experimental waveforms of V_{Ao}, V_{Bo}, V_{Co} and their sum V_{ao} match with the simulated waveforms presented in Fig. 10(f)–(i). Thus, the results of Fig. 14 have experimentally validated the open-loop operation of the proposed MIMC. However, to improve the quality of the output current I_{ao}, shown in Fig. 14(a), and to enhance the degree of controllability, a current controller must be added.

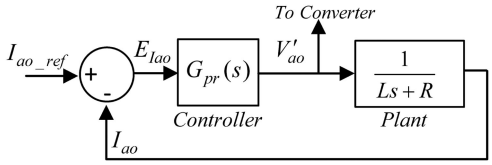

Fig. 15. PR current controller for MIMC.

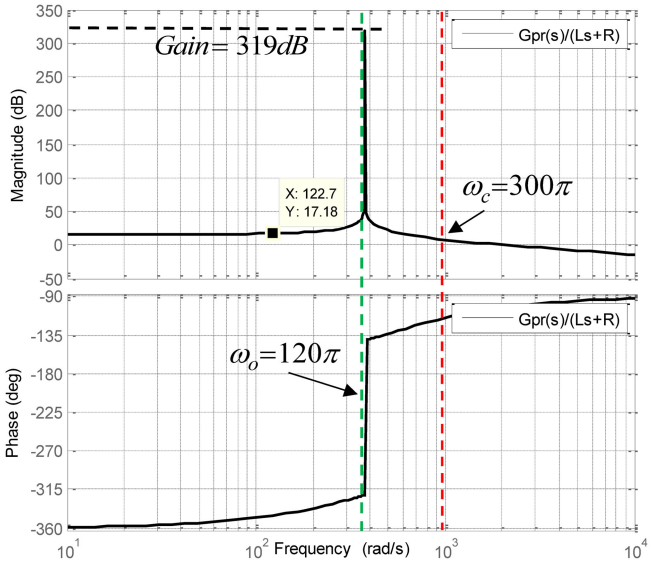

Fig. 16. Bode diagram of the current loop gain $\frac{G_{pr}(s)}{Ls+R}$.

A. Current Control Design

A proportional-resonant (PR) current controller was implemented as it can offer sinusoidal current reference I_{ao_ref} tracking. Moreover, thanks to the periodic-disturbance rejection capability [41], the commutation-related disturbances can be mitigated to enhance the quality of output current I_{ao}. The transfer function of the PR controller [41] is given in (18) and the controller diagram is illustrated in Fig. 15 where V'_{ao} is the required output voltage to track the reference current I_{ao_ref}. The required output voltage V'_{ao} is fed to the MIMC's duty cycle (4). A Bode plot of the loop gain of the designed current controller is shown in Fig. 16

$$G_{pr}(s) = \frac{2L\omega_c s^2 + (L{\omega_c}^2 + 2R\omega_c)s + R{\omega_c}^2}{s^2 + {\omega_o}^2}. \qquad (18)$$

A discretized version of the designed controller was implemented in the experimental rig and the recorded experimental waveforms of the output voltage V_{ao} with and without controller are presented in Fig. 17(a). Looking closely at the waveforms of V_{ao}, it can be observed that the distortion is reduced in output voltage V_{ao} when control loop is active but the improvement is not very clear because the output voltage V_{ao} is a pulsewidth modulated waveform. Therefore, for a clear comparison and to demonstrate the effectiveness of PR controller for MIMC, the output current in open loop I_{ao_open} is compared with the one in closed loop I_{ao_closed} in Fig. 17(b). As expected, Fig. 17(b) indicates that there is an enhancement in the quality of the output current I_{ao_closed} with the PR controller. To quantify this

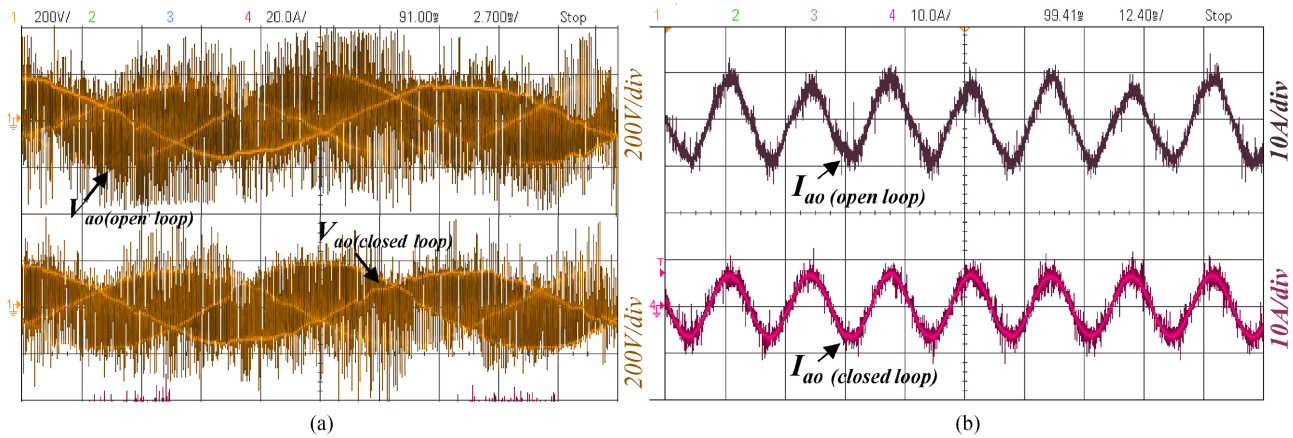

Fig. 17. Experimental waveforms at the output terminals of MIMC with and without closed-loop PR controller. (a) Output voltage V_{ao} with and without controller. (b) Output current I_{ao} with and without controller.

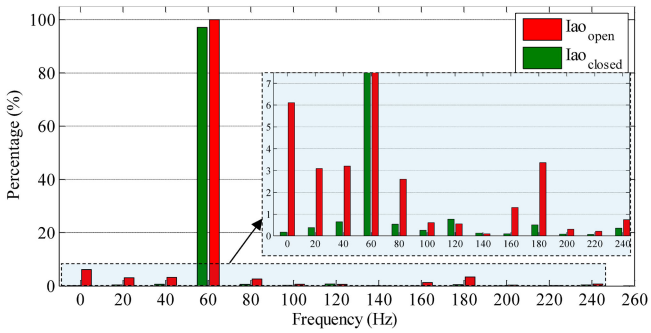

Fig. 18. FFT spectrums of output current I_{ao} in open and closed loop systems with fixed output filter inductance, i.e., L =10 mH.

improvement, the FFTs of both currents I_{ao_open} and I_{ao_closed} have been shown in Fig. 18. From Fig. 18, it can be seen that fundamental output frequency and the low-order harmonics, which were present in the open-loop system, are compensated by the PR controller. Although maximum gain of PR controller is at resonant frequency $\omega_o = 120\pi$ rad/s or $f_o = 60$ Hz, the gain at low frequencies and at multiples of the fundamental is still non negligible and allows a partial compensation of the undesired components. A peak THD of 8.70% and an average THD of 5% were recorded in I_{ao_open} whereas a peak THD of 1.71% and an average THD of 1.52% were observed in I_{ao_closed}. Note that a single PR controller was implemented as the main scope of the paper is validation of the MIMC's operation. However, to achieve higher control performances, a more sophisticated controller can be used to enhance the compensation capabilities at higher frequencies.

Furthermore, the response of the closed-loop system as a result of step change in current reference $I_{ao\_ref\_pk}$ from 3 to 2 A, was observed and recorded. The experimental waveforms are presented in Fig. 19(b). It can be noted from Fig. 19(b) that the system is stable and tracks the reference current I_{ao_ref}. Matching simulation results are presented in Fig. 19(a)–(c). A zoomed view of highlighted region of Fig. 19(a) and (b), presented in Fig. 19(c) and (d), shows the transient response of controller in simulation and experiment. Fig. 19(d) has some additional distortions near the zero crossing of the current, i.e,

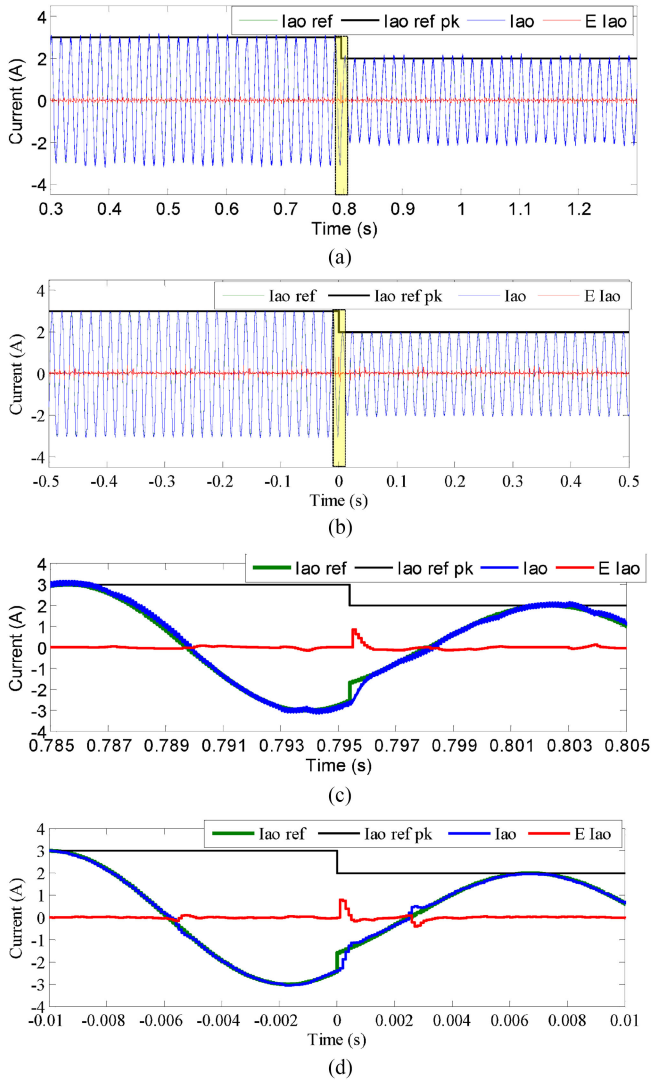

Fig. 19. Response of the closed-loop PR current-controller in a three-phase to single-phase MIMC topology. (a) and (b) a step-change in output current reference I_{ao_ref} from 3 to 2 A. (c) and (d) zoom of region highlighted in (a) and (b), showing the error E_{Iao} compensation during transient due to step-change in $I_{ao\_ref\_pk}$. (a) Step change—simulation. (b) Step change—experiment. (c) Transient—simulation. (d) Transient—experiment.

at $t = -5$ ms and $t = 3$ ms which is due to the sign of the current I_{ao} being detected incorrectly when the magnitude is too small, causing the selection of wrong commutation path in the FSM of Fig. 8. This is due to the limitations of the sign detection hardware (shown in Fig. 12). However, the controller is taking necessary action to compensate these distortions. The reason why the same distortions are not present in the simulation result of Fig. 19(c) is that an ideal sign block is used in the simulation model.

VI. Conclusion

This paper has presented a comprehensive study on modulation, commutation, and control methods for a MIMC topology. The experimental results have validated the conceptual MIMC topology, demonstrating its practical feasibility. The design and implementation of the modulation for the MIMC topology is derived from a generalization of standard modulation methods used in matrix converters. Instead, commutation between states is particularly challenging because of the leakage inductance of the MF transformer that provides isolation to the topology. However, the paper demonstrated that the implementation of a leakage-inductance-tolerant commutation enables a safe operation of the converter also in a practical scenario. The proposed MIMC topology can find its ac–ac applications where weight and volume are the main priority, i.e., in traction applications and grid applications with space restrictions.

Appendix
Derivation of Transformer Voltage V_{TK} and Cell Voltage V_{Ko}

The transformer voltage of the first cell, i.e., $V_{TA}(t)$ is function of input voltage V_{Ai} and 50% duty-cycle square wave $s(t)$, therefore, can be expressed as (21) which can be simplified to (23). The generalized form of transformer voltage V_{TK}, given in (12), can be obtained by similar approach

$$V_{Ai}(t) = V_m \sin(\omega_i t) \tag{19}$$

$$s(t) = \frac{4}{\pi} \sum_{n=1,3,5,\ldots}^{\infty} \left[\frac{1}{n} \sin(n\omega_s t) \right] \tag{20}$$

$$V_{TA}(t) = V_{Ai}(t) s(t) \tag{21}$$

$$V_{TA}(t) = \frac{4V_m}{\pi} \sum_{n=1,3,5,\ldots}^{\infty} \left[\frac{1}{n} \sin(\omega_i t) \sin(n\omega_s t) \right] \tag{22}$$

$$V_{TA}(t) = \frac{2V_m}{\pi} \sum_{n=1,3,5,\ldots}^{\infty} \frac{1}{n} \times \left[\cos(n\omega_s t - \omega_i t) - \cos(n\omega_s t + \omega_i t) \right]. \tag{23}$$

The output voltage of the first cell i.e., $V_{Ao}(t)$ is function of duty cycle D_{Aa} and input voltage V_{Ai}, therefore, can be expressed as (25). Substitution of (19) and (24) to (25), yields (26), which is simplified to form (28) after trigonometric manipulation. Following the same approach, a generalized expression of (13) representing all cell output voltages V_{Ko} is determined

$$D_{Aa}(t) = \frac{1}{3} \left(1 + 2\, q \sin(\omega_i t) \sin(\omega_o t) \right) \tag{24}$$

$$V_{Ao}(t) = V_{Ai}(t) D_{Aa}(t) \tag{25}$$

$$V_{Ao}(t) = \frac{V_m}{3} \sin(\omega_i t) \left[1 + 2\, q \sin(\omega_i t) \sin(\omega_o t) \right] \tag{26}$$

$$V_{Ao}(t) = \frac{V_m}{3} \sin(\omega_i t) + \frac{qV_m}{3} \sin(\omega_o t) \left[1 - \cos(2\omega_i t) \right] \tag{27}$$

$$V_{Ao}(t) = \frac{V_m}{3} \sin(\omega_i t) + \frac{qV_m}{6} \sin(2\omega_i t - \omega_o t) - \frac{qV_m}{6} \sin(2\omega_i t + \omega_o t) + \frac{qV_m}{3} \sin(\omega_o t). \tag{28}$$

References

[1] A. Alesina and M. G. B. Venturini, "Analysis and design of optimum-amplitude nine-switch direct ac–ac converters," *IEEE Trans. Power Electron.*, vol. 4, no. 1, pp. 101–112, Jan. 1989.

[2] P. W. Wheeler, J. Rodriguez, J. C. Clare, L. Empringham, and A. Weinstein, "Matrix converters: A technology review," *IEEE Trans. Ind. Electron.*, vol. 49, no. 2, pp. 276–288, Apr. 2002.

[3] T. Friedli, J. W. Kolar, J. Rodriguez, and P. W. Wheeler, "Comparative evaluation of three-phase ac–ac matrix converter and voltage dc-link back-to-back converter systems," *IEEE Trans. Ind. Electron.*, vol. 59, no. 12, pp. 4487–4510, Dec. 2012.

[4] M. Galea, G. Buticchi, L. Empringham, L. D. Lillo, and C. Gerada, "Design of a high-force-density tubular motor," *IEEE Trans. Industry Appl.*, vol. 50, no. 4, pp. 2523–2532, Jul./Aug. 2014.

[5] S. Bifaretti, P. Zanchetta, A. Watson, L. Tarisciotti, and J. C. Clare, "Advanced power electronic conversion and control system for universal and flexible power management," *IEEE Trans. Smart Grid*, vol. 2, no. 2, pp. 231–243, Jun. 2011.

[6] S. F. Pinto, P. Alcaria, J. Monteiro, and J. F. Silva, "Matrix converter-based active distribution transformer," *IEEE Trans. Power Del.*, vol. 31, no. 4, pp. 1493–1501, Aug. 2016.

[7] J. E. Huber and J. W. Kolar, "Solid-state transformers: On the origins and evolution of key concepts," *IEEE Ind. Electron. Mag.*, vol. 10, no. 3, pp. 19–28, Sep. 2016.

[8] J. E. Huber and J. Kolar, "Applicability of solid-state transformers in today's and future distribution grids," *IEEE Trans. Smart Grid*, vol. 10, no. 1, pp. 317–326, Jan. 2019.

[9] D. Dujic, F. Kieferndorf, F. Canales, and U. Drofenik, "Power electronic traction transformer technology," in *Proc. 7th Int. Power Electron. Motion Control Conf.*, 2012, vol. 1, pp. 636–642.

[10] P. Drabek, Z. Peroutka, M. Pittermann, and M. Cedl, "New configuration of traction converter with medium-frequency transformer using matrix converters," *IEEE Trans. Ind. Electron.*, vol. 58, no. 11, pp. 5041–5048, Nov. 2011.

[11] A. Q. Huang, "Medium-voltage solid-state transformer: Technology for a smarter and resilient grid," *IEEE Ind. Electron. Mag.*, vol. 10, no. 3, pp. 29–42, Sep. 2016.

[12] H. Chen and D. Divan, "Design of a 10 kVA soft-switching solid state transformer (S4T)," *IEEE Trans. Power Electron.*, vol. 33, no. 7, pp. 5724–5738, Jul. 2018.

[13] W. McMurray, "Power converter circuits having a high-frequency link," U.S. Patent 3517300, Jun. 23, 1970.

[14] S. Falcones, R. Ayyanar, and X. Mao, "A dc–dc multiport-converter-based solid-state transformer integrating distributed generation and storage," *IEEE Trans. Power Electron.*, vol. 28, no. 5, pp. 2192–2203, May 2013.

[15] S. Xu, A. Q. Huang, and R. Burgos, "Review of solid-state transformer technologies and their application in power distribution systems," *IEEE J. Emerg. Sel. Topics Power Electron.*, vol. 1, no. 3, pp. 186–198, Sep. 2013.

[16] H. S. Krishnamoorthy, P. Enjeti, and J. J. Sandoval, "Solid state transformer for grid interface of high power multi-pulse rectifiers," *IEEE Trans. Industry Appl.*, vol. 54, no. 5, pp. 5504–5511, Sep./Oct. 2018.

[17] Y. Liu, Y. Liu, H. Abu-Rub, B. Ge, R. S. Balog, and Y. Xue, "Model predictive control of a matrix-converter based solid state transformer for utility grid interaction," in *Proc. IEEE Energy Convers. Congress Expo.*, 2016, pp. 1–6.
[18] J. J. Sandoval, S. Essakiappan, and P. Enjeti, "A bidirectional series resonant matrix converter topology for electric vehicle dc fast charging," in *Proc. IEEE Appl. Power Electron. Conf. Expo.*, 2015, pp. 3109–3116.
[19] A. Rufer, N. Schibli, C. Chabert, and C. Zimmermann, "Configurable front-end converters for multicurrent locomotives operated on 16 2/3 Hz ac and 3 kV dc systems," *IEEE Trans. Power Electron.*, vol. 18, no. 5, pp. 1186–1193, Sep. 2003.
[20] H. Chen, A. Prasai, R. Moghe, K. Chintakrinda, and D. Divan, "A 50 kVA three-phase solid state transformer based on the minimal topology: Dyna-c," *IEEE Trans. Power Electron.*, vol. 31, no. 12, pp. 8126–8137, Dec. 2016.
[21] H. Qin and J. W. Kimball, "Solid-state transformer architecture using ac–ac dual-active-bridge converter," *IEEE Trans. Ind. Electron.*, vol. 60, no. 9, pp. 3720–3730, Sep. 2013.
[22] H. Chen and D. Divan, "Soft-switching solid-state transformer (s4t)," *IEEE Trans. Power Electron.*, vol. 33, no. 4, pp. 2933–2947, Apr. 2018.
[23] K. Basu, A. Shahani, A. K. Sahoo, and N. Mohan, "A single-stage solid-state transformer for PWM ac drive with source-based commutation of leakage energy," *IEEE Trans. Power Electron.*, vol. 30, no. 3, pp. 1734–1746, Mar. 2015.
[24] K. Basu and N. Mohan, "A single-stage power electronic transformer for a three-phase PWM ac/ac drive with source-based commutation of leakage energy and common-mode voltage suppression," *IEEE Trans. Ind. Electron.*, vol. 61, no. 11, pp. 5881–5893, Nov. 2014.
[25] D. Boroyevich, I. Cvetkovi, D. Dong, R. Burgos, F. Wang, and F. Lee, "Future electronic power distribution systems a contemplative view," in *Proc. 12th Int. Conf. Optim. Elect. Electron. Equip.*, 2010, pp. 1369–1380.
[26] R. Silversides, T. Green, and M. M. C. Merlin, "A high density converter for mid feeder voltage regulation of low voltage distribution feeders," in *Proc. IEEE Energy Convers. Congr. Expo.*, 2014, pp. 1972–1978.
[27] Y. Sun, W. Xiong, M. Su, H. Dan, X. Li, and J. Yang, "Modulation strategies based on mathematical construction method for multimodular matrix converter," *IEEE Trans. Power Electron.*, vol. 31, no. 8, pp. 5423–5434, Aug. 2016.
[28] U. Nasir, M. Rivera, A. Costabeber, and P. Wheeler, "A Venturini based modulation technique for a new isolated ac/ac power converter," in *Proc. 42nd Annu. Conf. IEEE Ind. Electron. Soc.*, 2016, pp. 6243–6248.
[29] M. Kang, P. N. Enjeti, and I. J. Pitel, "Analysis and design of electronic transformers for electric power distribution system," *IEEE Trans. Power Electron.*, vol. 14, no. 6, pp. 1133–1141, Nov. 1999.
[30] C. Daolian and L. Lei, "Bi-polarity phase-shifted controlled voltage mode ac/ac converters with high frequency ac link," in *Proc. IEEE 34th Annu. Conf. Power Electron. Specialist*, 2003, pp. 677–682.
[31] C. Daolian and L. Jian, "The uni-polarity phase-shifted controlled voltage mode ac-ac converters with high frequency ac link," *IEEE Trans. Power Electron.*, vol. 21, no. 4, pp. 899–905, Jul. 2006.
[32] L. Lei and Z. Qinglong, "Comparisons of two kinds of ac/ac converters with high frequency link," in *Proc. 34th Annu. Conf. IEEE Ind. Electron. Soc.*, 2008, pp. 618–622.
[33] N. Burany, "Safe control of four-quadrant switches," in *Proc. Conf. Record IEEE Industry Appl. Soc. Annu. Meeting*, 1989, vol. 1, pp. 1190–1194.
[34] B. Wang and E. Sherif, "Spectral analysis of matrix converters based on 3-D Fourier integral," *IEEE Trans. Power Electron.*, vol. 28, no. 1, pp. 19–25, Jan. 2013.
[35] U. Nasir, A. Costabeber, M. Rivera, P. Wheeler, and J. Clare, "A leakage-inductance-tolerant commutation strategy for isolated ac/ac converters," *IEEE J. Emerg. Sel. Topics Power Electron.*, vol. 7, no. 1, pp. 467–479, Mar. 2019.
[36] D. Chen and Y. Chen, "Step-up ac voltage regulators with high-frequency link," *IEEE Trans. Power Electron.*, vol. 28, no. 1, pp. 390–397, Jan. 2013.
[37] H. Krishnaswami and V. Ramanarayanan, "Control of high-frequency ac link electronic transformer," *IEE Proc. Electric Power Appl.*, vol. 152, no. 3, pp. 509–516, May 2005.
[38] H. Keyhani, H. A. Toliyat, M. Harfman-Todorovic, R. Lai, and R. Datta, "An isolated resonant ac-link three-phase ac–ac converter using a single HF transformer," *IEEE Trans. Ind. Electron.*, vol. 61, no. 10, pp. 5174–5183, Oct. 2014.
[39] F. H. Khan, L. M. Tolbert, and W. E. Webb, "Hybrid electric vehicle power management solutions based on isolated and nonisolated configurations of multilevel modular capacitor-clamped converter," *IEEE Trans. Ind. Electron.*, vol. 56, no. 8, pp. 3079–3095, Aug. 2009.
[40] K. Yamada *et al.*, "Integrated filters and their combined effects in matrix converter," in *Proc. 40th IAS Annu. Meeting. Conf. Record Industry Appl. Conf*, Oct. 2005, vol. 2, pp. 1406–1413.
[41] A. Kuperman, "Proportional-resonant current controllers design based on desired transient performance," *IEEE Trans. Power Electron.*, vol. 30, no. 10, pp. 5341–5345, Oct. 2015.

Usman Nasir (S'13) received the B.Sc. degree in electrical engineering from the National University of Sciences and Technology, Islamabad, Pakistan, in 2013, and the M.Sc. degree in electric power system and its automation from North China Electric Power University, Beijing, China, in 2015. He is currently working toward the Ph.D. degree in electrical engineering at the Power Electronics and Machine Control Research Group, University of Nottingham, Nottingham, U.K.

His current research interests include new matrix converter-based topologies, novel commutation algorithms, new modulation techniques, model predictive control for converters, and high-power density SiC converters.

Mr. Nasir is a recipient of the Dean of Engineering Scholarship for International Research Excellence for the Ph.D. studies. He received the Best Paper Award from the IEEE Southern Power Electronics Conference 2017, Chile.

Alessandro Costabeber (S'09–M'13) received the M.Sc. degree (Hons.) in electronic engineering and the Ph.D. degree in information engineering from the University of Padova, Padua, Italy, in 2008 and 2012, respectively. His Ph.D. thesis was on energy-efficient architectures and control for future residential microgrids.

In 2014, he joined as a Lecturer in power electronics with the Power Electronics and Machine Control Research Group, University of Nottingham, Nottingham, U.K. His current research interests include modular multilevel converters for HVDC, high-power density converters, and control and stability analysis of ac and dc microgrids.

Dr. Costabeber received the IEEE Joseph John Suozzi INTELEC Fellowship Award in Power Electronics in 2011.

Patrick Wheeler (M'01–SM'10) received the B.Eng. (Hons.) degree in electrical engineering from the University of Bristol, Bristol, U.K., in 1990, and the Ph.D. degree in electrical engineering for his work on matrix converters from the same university, in 1994.

In 1993, he moved to the University of Nottingham and worked as a Research Assistant with the Department of Electrical and Electronic Engineering. In 1996, he became a Lecturer in the Power Electronics, Machines, and Control Group, the University of Nottingham, U.K. Since January 2008, he has been a Full Professor with the same research group. From 2015 to 2018, he was the Head of the Department of Electrical and Electronic Engineering, the University of Nottingham. He is currently the Head of the Power Electronics, Machines, and Control Research Group, Global Director of the University of Nottingham's Institute of Aerospace Technology, and is the Li Dak Sum Chair Professor in electrical and aerospace engineering. He has authored and coauthored 500 academic publications in leading international conferences and journals.

Prof. Wheeler is a member of the PELs AdCom and was an IEEE PELs Distinguished Lecturer from 2013 to 2017.

Marco Rivera (S'09–M'11) received the B.Sc. degree in electronics engineering and the M.Sc. degree in electrical engineering from the Universidad de Concepción, Concepción, Chile, in 2007 and 2008, respectively, and the Ph.D. degree from the Department of Electronics Engineering, Universidad Técnica Federico Santa Mar ± a, Valpara ± so, Chile, in 2011.

He is currently a Professor with the Department of Electrical Engineering, Universidad de Talca, Curicó, Chile. His current research interests include matrix converters, predictive and digital controls for high-power drives, four-leg converters, and the development of high-performance control platforms based on field-programmable gate arrays.

Dr. Rivera was the recipient of the Premio Tesis de Doctorado Academia Chilena de Ciencias 2012 in 2013 for his best Ph.D. dissertation developed in 2011 for national and foreign students in any exact or natural sciences program that is a member of the Academia Chilena de Ciencias, Chile. He was also the recipient of the Outstanding Engineer of 2015 Award from the Chilean Association of Electrical and Electronics Industry and the IEEE-Chile, and a scholarship from the Chilean Research Fund CONICYT for his Ph.D. studies.

Jon Clare (M'90–SM'04) was born in Bristol, U.K., in 1957. He received the B.Sc. and Ph.D. degrees in electrical engineering from the University of Bristol, Bristol, U.K., in 1979 and 1983, respectively.

From 1984 to 1990, he was a Research Assistant and Lecturer with the University of Bristol, where he was involved in teaching and research on power electronic systems. Since 1990, he has been with the Power Electronics, Machines, and Control Group, University of Nottingham, Nottingham, U.K., where he is currently a Professor of Power Electronics and the Head of the Department of Electronic and Electrical Engineering. His research interests include power-electronic converters and modulation strategies, variable-speed-drive systems, and electromagnetic compatibility.